
Article:
Arciniegas, Milena P., Castelli, Andrea, Brescia, Rosaria et al. (6 more authors) (2020) Unveiling the Dynamical Assembly of Magnetic Nanocrystal Zig-Zag Chains via In Situ TEM Imaging in Liquid. Small. e1907419. ISSN 1613-6810

https://doi.org/10.1002/smll.201907419

NANO · MICRO small
www.small-journal.com

Unveiling the Dynamical Assembly of Magnetic Nanocrystal Zig-Zag Chains via In Situ TEM Imaging in Liquid

Milena P. Arciniegas, Andrea Castelli, Rosaria Brescia, David Serantes,* Sergiu Ruta, Ondrej Hovorka, Akira Satoh, Roy Chantrell, and Teresa Pellegrino*

The controlled assembly of colloidal magnetic nanocrystals is key to many applications such as nanoelectronics, storage memory devices, and nanomedicine. Here, the motion and ordering of ferrimagnetic nanocubes in water via liquid-cell transmission electron microscopy is directly imaged in situ. Through the experimental analysis, combined with molecular dynamics simulations and theoretical considerations, it is shown that the presence of highly competitive interactions leads to the formation of stable monomers and dimers, acting as nuclei, followed by a dynamic growth of zig-zag chain-like assemblies. It is demonstrated that such arrays can be explained by first, a maximization of short-range electrostatic interactions, which at a later stage become surpassed by magnetic forces acting through the easy magnetic axes of the nanocubes, causing their tilted orientation within the arrays. Moreover, in the confined volume of liquid in the experiments, interactions of the nanocube surfaces with the cell membranes, when irradiated at relatively low electron dose, slow down the kinetics of their self-assembly, facilitating the identification of different stages in the process. The study provides crucial insights for the formation of unconventional linear arrays made of ferrimagnetic nanocubes that are essential for their further exploitation in, for example, magnetic hyperthermia, magneto-transport devices, and nanotheranostic tools.

Anisotropic colloidal nanocrystals (NCs) are important LEGO-like bricks characterized by the richness of geometries into which they can self-assemble.[1] This ability has many interesting implications for their use as nanocomponents in a broad range of applications, from optics, electronics to medicine.[2] The desired functionality of the assemblies can be achieved by changing their configuration. For example, linear arrays are the target geometry for electronic circuits, while ordered films are required for plasmonics.[3] Importantly, the observed diversity in the assembled geometries is the result of the careful tuning of interactions among NCs (e.g., electrostatic, magnetic dipoles, capillary, and van der Waals), in particular for anisotropic shaped ones. The delicate interplay between attractive and repulsive forces depends on both particle shape and ligand coating, which determine the spatial location and orientation of the particles when embedded within highly complex superstructures.[1b,c,4] Clearly, controlling the interparticle interactions and, in particular, their relation to the microscopic physical configuration, represents not only an important scientific challenge, but also a potential means of optimizing the functionality of NCs.

An exemplary case of competitive interactions is found in the assemblies of cubic-shaped NCs that are endowed with magnetic properties.[5] Such structures are the focus of active research primarily in the field of biomedicine due to their important role as heat mediators in cancer hyperthermia therapy[6] and as contrast agents for imaging and diagnosis,[7] in particular when they exhibit ordered structures.[5a,8] The assembly of nanocubes is typically driven by short-range interactions that maximize face-to-face contact, forming closely packed structures.[9] This can be understood from the presence of attractive forces that

Dr. M. P. Arciniegas, Dr. A. Castelli, Dr. R. Brescia, Dr. T. Pellegrino
Istituto Italiano di Tecnologia
Via Morego 30, Genova 16163, Italy
E-mail: Milena.Arciniegas@iit.it
Dr. D. Serantes
Applied Physics Department and Instituto de Investigacións Tecnolóxicas
Universidade de Santiago de Compostela
Santiago de Compostela 15782, Spain
E-mail: David.Serantes@usc.es
The ORCID identification number(s) for the author(s) of this article can be found under https://doi.org/10.1002/smll.201907419.

DOI: 10.1002/smll.201907419

Dr. S. Ruta, Prof. R. Chantrell
Department of Physics
University of York
York YO10 5DD, UK
Dr. O. Hovorka
Faculty of Engineering and Physical Sciences
University of Southampton
Southampton SO16 7QF, UK
Prof. A. Satoh
Faculty of System Science and Technology
Akita Prefecture University
Yurihonjo 015-0055, Japan

originate from the ligands coating the nanocube surfaces. This symmetry is dominant in many cases, even when an external field is applied to the nanocubes and the long-range ordering follows the directionality of the guiding force.[10] Breaking this symmetry to enable the formation of more exotic configurations can be attained by favoring the alignment of nanocubes from their corners.[11] This is a condition that, in principle, is possible to achieve from magnetic nanocubes when generating an effective strength of dipole–dipole interaction since this acts through the nanocube magnetic easy axis, which is conveniently directed along the cube body diagonal. Such 1D self-assembled structures have been observed so far from polymer-grafted Ag plasmonic nanocubes[11] and from Fe_3O_4 magnetic nanocubes.[5c,12] However, the elucidation of the physical principles behind the formation of such structures, in particular from magnetic interactions, remains an unanswered challenge.

Although computational simulations have significantly improved our understanding of the assembly mechanisms of magnetic nanocubes,[12,13] a direct experimental visualization of the process is still missing. Transmission electron microscopy (TEM) analyses of colloidal NCs within a liquid, with its capability to monitor in situ shape, orientation and position of nanostructures, is an appropriate technique to conduct such visual experiments.[14] Despite that the TEM imaging is in itself informative, the dynamical assembly behavior must be driven by the energies involved in the assembly formation. The question is if this information can be extracted from the experimental data. Recent technological advances have allowed the exploration of processes occurring directly in the liquid phase.[15] The in situ observation of NC self-assembly in their natural environment, while demonstrated for a few cases of NCs of complex shapes,[16] has not been yet reported for magnetic NCs, most likely because of the presence of multiple interactions, some of which are highly sensitive to the electron beam,[17] adding further complexity to the experiments.

Here, with a combination of in situ liquid TEM experiments on a well-known nanosystem and computational/theoretical models, we develop the framework in which quantitative information can be determined. Specifically, we investigate the self-organization of magnetic NCs by confining them in between two electron-transparent membranes in a liquid cell TEM holder, obtaining a detailed picture of their assembly behavior while irradiated by an electron beam. We chose to investigate polymer-coated ferrimagnetic $Co_{0.7}Fe_{2.3}O_4$ nanocubes that were dispersed in water as a system known for self-assembly into linear arrays, leading to superior heating performance for cancer nanotheranostic therapy.[18] Our in situ chain formation experiments are fully supported by computational and theoretical modelling, which allow estimation of the energy barriers governing the nanocube chain organization from direct fits to experimental data. We reveal a hierarchy of nanocube interactions, beginning with the formation of nucleation centers. Subsequently, these stable nuclei start to attract additional nanocubes from the surrounding volume of liquid and form chain-like structures. Surprisingly, instead of the usual face-to-face contact among nanocubes, the particles adopt a tilted configuration within the assemblies, favoring an unusual edge-to-edge NC contact that results in zig-zag arrays anchored to the cell membrane. We interpret these findings through a two-step route: first, strong electrostatic forces between the negatively charged surface of the nanocubes and the upper cell membrane, which increase with the duration of the electron beam exposure, i.e., with the increasing electron dose. The nucleation process approaches saturation over time and dominant magnetic interactions explain the subsequent formation of linear arrays, as confirmed using Monte Carlo modelling. Our study thus provides a quantitative understanding of the assembly mechanism of magnetic NCs into unusual configurations and elucidates the nature of the different interactions involved in the process. This is highly significant given the potential role of oriented structures in developing and optimizing the functionalities of magnetic nanocube such as magnetic hyperthermia, delivery systems, storage memory devices, and magneto-transport devices.

We prepared ferrimagnetic $Co_{0.7}Fe_{2.3}O_4$ nanocubes coated with poly maleic anhydride 1-octadecene (PMAO) and dispersed them in water following our standard protocols (see details on Section S1, Supporting Information).[18,19] A simplistic representation of the nanocube's surface is shown in **Figure 1**a, which includes the anchorage of the polymeric coating layer. The nanocubes have an edge length, *l*, of around 27 nm with a coating layer of ≈2 nm, as measured by TEM analyses, and a slightly higher hydrodynamic size if considering the dynamic light scattering (DLS) measurements (Figure S1, Supporting Information). The nanocubes have a spinel ferrite crystal structure and their facets are formed by {100} planes, as detailed in a previous work from our group,[18] which also include a full characterization of their magnetic properties.

Figure 1b displays a scanning electron microscopy (SEM) image of the dried nanocubes deposited on a Si substrate via drop casting from an aqueous solution. In this condition, we observe that the nanocubes remain loosely packed and adopt principally a face-to-face configuration with neighboring nanocubes, one of the possible NC–NC contacts adopted by nanocubes within their assemblies. A sketch of the geometry of the liquid-cell TEM experiment is shown in Figure 1c and the inset illustrates the possible assembled configurations of the nanocubes. The figure includes a zoom-in view of a single nanocube highlighting the negatively charged surfaces and easy magnetic axes, *m*, (red arrow). Indeed, polymer coated nanocubes have a negative charge surface as confirmed by their Z-potential value of −25.8 ± 1.5 mV. Note that the Si_3N_4 electron transparent membranes were treated by an oxygen-containing plasma immediately before use, inducing negatively charged surfaces. The liquid cell was loaded in a specialized holder and inserted in a TEM for analysis as detailed in the Experimental Section. All the Supporting Information Movies are played at 5 frame per second (fps) and the corresponding irradiation times provided in the time-lapse TEM images in the figures.

In a typical experiment, the TEM image focus (i.e., the objective lens current) was set on an area of the top membrane close to the edge of the electron-transparent area. Using the top membrane as a focal plane facilitates the recognition of nanocrystal at single particle resolution in the FOV when they come close to it by changes on their contrast. The beam was then blanked for few minutes and relocated in a region of interest. The analysis of the nanocubes in water was performed with two different electron dose rates, 0.55 ± 0.04 and 1.40 ± 0.14 $e^- Å^{-2} s^{-1}$. These are low dose values if one compares them, for example, with the

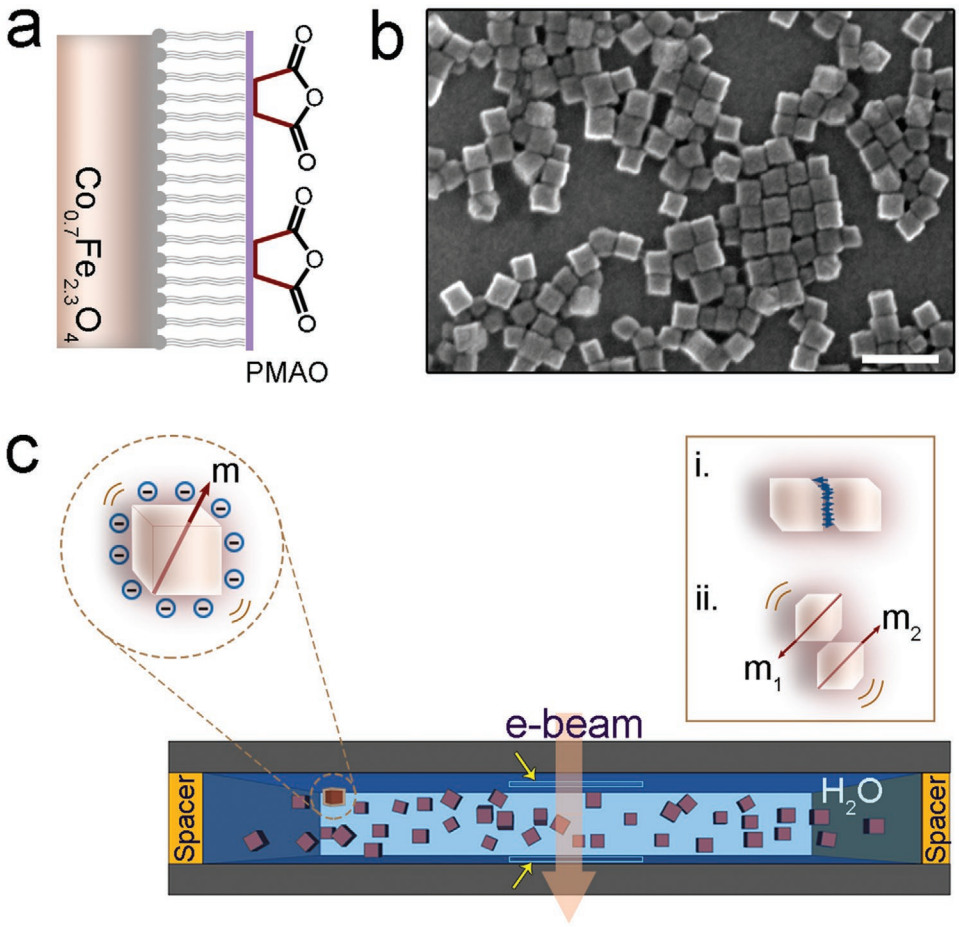

Figure 1. PMAO-coated $Co_{0.7}Fe_{2.3}O_4$ ferrimagnetic nanocubes. a) Representation of the nanocube surface stabilized by the polymer layer. b) SEM image of nanocubes standing on a Si substrate after drop casting a water suspension of the nanocubes and water evaporation. Scale bar: 100 nm. c) Sketch of a liquid cell loaded with aqueous solution of nanocubes, as used in the experiments. The yellow arrows indicate the Si_3N_4 electron transparent membranes. The zoom-in of a nanocube in the sketch highlights the negative surface charge of the particle and the easy magnetic axis, *m*, along the body diagonal. The insets i,ii) display two possible nanocube configurations in their assemblies: i) face-to-face induced by shape anisotropy and ii) edge-to-edge driven by pure magnetic interactions.

doses used in experiments targeting the monitoring of reactions, which usually work with elevated electron beam dose to trigger the mechanisms.[20] In our case, the use of low-dose is aimed mainly at reducing the potential radiation damage to the nanocubes while imaging them using TEM. These values are in agreement with the electron dose rates used for the observation of self-assembly process in complex systems in aqueous solution.[21] We initially inspected the liquid layer at a relatively low electron dose rate ($DR_1 = 0.55 \pm 0.04$ e^- $Å^{-2}$ s^{-1}) and observed the motion of nanocubes, appearing in the field of view (FOV) after 5 s of electron beam exposure (Movie S1, Supporting Information): the nanocubes can be identified when they are close to focus, thanks to their relatively sharp contour and relatively dark contrast with respect to the liquid, which appeared featureless at the beginning of the experiment, indicating an uniform liquid layer. We observed more nanocubes in focus in our FOV, emerging from the surrounding/underlying liquid over time, which is attributed to potential beam-induced charging of the membrane, as typically reported in similar studies.[16a,21a] We noticed that, after prolonged beam exposure, a few nanocubes began to persist, close to focus, in the FOV (Figure S2, Supporting Information), and eventually few elongated structures can be discerned at the end of Movie S1 (Supporting Information).

To better detail the sequence of events on the nanocubes motion, we investigated another pocket of liquid and imaged it closer and with a slightly higher dose rate ($DR_2 = 1.40 \pm 0.14$ e^- $Å^{-2}$ s^{-1}). **Figure 2** shows a series of zero-loss filtered bright field (BF)-TEM images extracted from Movie S2 (Supporting Information) that follows the motion and aggregation of the nanocubes in real time under these conditions. It shows a continuous free movement of nanocubes with a diffuse contrast in the FOV (of ≈1.6 × 1.6 μm^2) for the first 10 s. For comparison, we show in Movie S3 (Supporting Information) a view of the nanocubes when located in a dried liquid cell in two different regions containing different numbers of nanocubes (Figure S3, Supporting Information). In the liquid cell, suddenly, single nanocubes (named here "monomers") pop up to the top membrane in a few seconds at random locations in the FOV (see Figure 2a), as it was also observed in the movie recorded at low electron beam dose. Interestingly, most

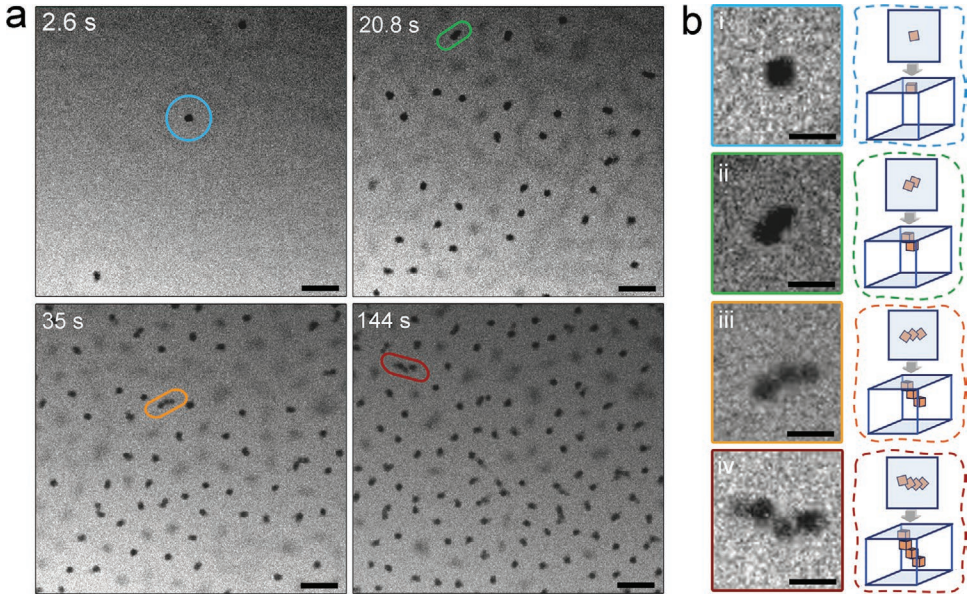

Figure 2. In situ TEM observations of PMAO-coated $Co_{0.7}Fe_{2.3}O_4$ nanocubes in water. Selected snapshot extracted from Movie S2 (Supporting Information) showing the evolution of the nanocubes toward linear arrays. a) Single nanocubes appear in the FOV after a few seconds of electron beam exposure (2.6 s), acting as nuclei for the formation of dimers over longer times (20.8 s). Trimers and longer linear arrays form with increasing time of exposure. b) Close view of a i) monomer, ii) dimer, iii) trimer, and iv) tetramer observed over time in the time-lapse images and framed in (a) in blue, green, orange, and red, respectively. Scale bars: a) 200 nm, b) 50 nm. The sketches near to each panel in (b) highlight the observed projections (top) of the nanocubes in the liquid (bottom).

of these monomers remain in their position over time, however they show different orientations in their TEM 2D projections (Figure S4, Supporting Information), indicating that the nanocubes are not immobilized on the top membrane, and thus they are still able to rotate in the liquid.

Such behavior can be explained by strong vertical bonding to the membrane under the effect of the electrostatic interactions without constraint of the rotational degrees of freedom in the plane of the membrane. With increasing observation time, single nanocubes continue to arrive in the inspected region, along with a few dimers (two nanocubes in contact), some of which move together (showing both a clear contrast) closer to the top membrane and remain in the FOV (see panel at 20.8 s in Figure 2a), while others retreat deeper into the liquid. The diffuse contrast observed around the nanocubes that appear in focus (and thus, close to the top membrane where we set the TEM image focus) is due to particles located deeper in the liquid where such objects continue to randomly move, as can be observed through the complete sequence of time-lapse images in Movie S2 (Supporting Information). After the initial monomer-cell membrane attraction, we observe elongated objects in the FOV over time. Initially, these are dimeric structures that appear most of them in focus. Subsequently, more neighboring nanocubes arrive closer to the stable dimers and longer structures, such as trimers (see panel at 35 s in Figure 2a) and tetramers (see panel at 144 s in Figure 2a), can be distinguished from the TEM 2D projections. We noticed that once formed, such structures, from dimers to tetramers, move together, indicating that the nanocubes within them are linked through strong attractive forces. This denotes that the observed linear arrays are not overlapped TEM 2D projections of random monomers. Figure 2b shows representative short and long chains of nanocubes observed in the FOV. Over time the assembled arrays stabilize with a maximum of five nanocubes per chain. As shown in the Movie S2 (Supporting Information), after 144 s of electron beam exposure, only few more nanocubes are incorporated in the FOV, and these continue their free motion deeper in the underlying liquid (blurry contrast), even at longer time of irradiation when the nanocubes appear locally damaged under the electron beam. At this final stage, the nanocubes show truncated corners surrounded by small fragments produced by the NC damage under the persistent exposure to the electron beam (see Movie S4, Supporting Information). The observed electron beam-induced degradation starts right from the corners of the nanocubes mimicking very well that reported for similar polymer-coated nanocubes of iron oxide in a biological environment.[22] This effect is likely due to the fact that the sharp corners are more reactive by having a less homogeneous coating layer, and thus the nanocube surface may be more exposed to the environment, in this case the electron beam.

To gain detailed information about the chain formation and the arrangement of nanocubes within chains, we selected different arrays and tracked their origin and evolution in the liquid cell. Complete FOV TEM images are shown in Figure S5 (Supporting Information) showing the selected objects framed in white. **Figure 3**a shows an example of the spontaneous self-assembly of a tetramer observed at 57.2 s in Movie S2 (Supporting Information), including the different stages of its evolution starting from a free monomer. The first free monomer initially approaches the top membrane at 39.2 s, as it is captured in the red-framed region, and becomes attracted to the membrane at about 39.4 s in Figure 3a.

Subsequently, the assembly process continues by the attachment of a second monomer at 45.2 s. Such dimer structures are

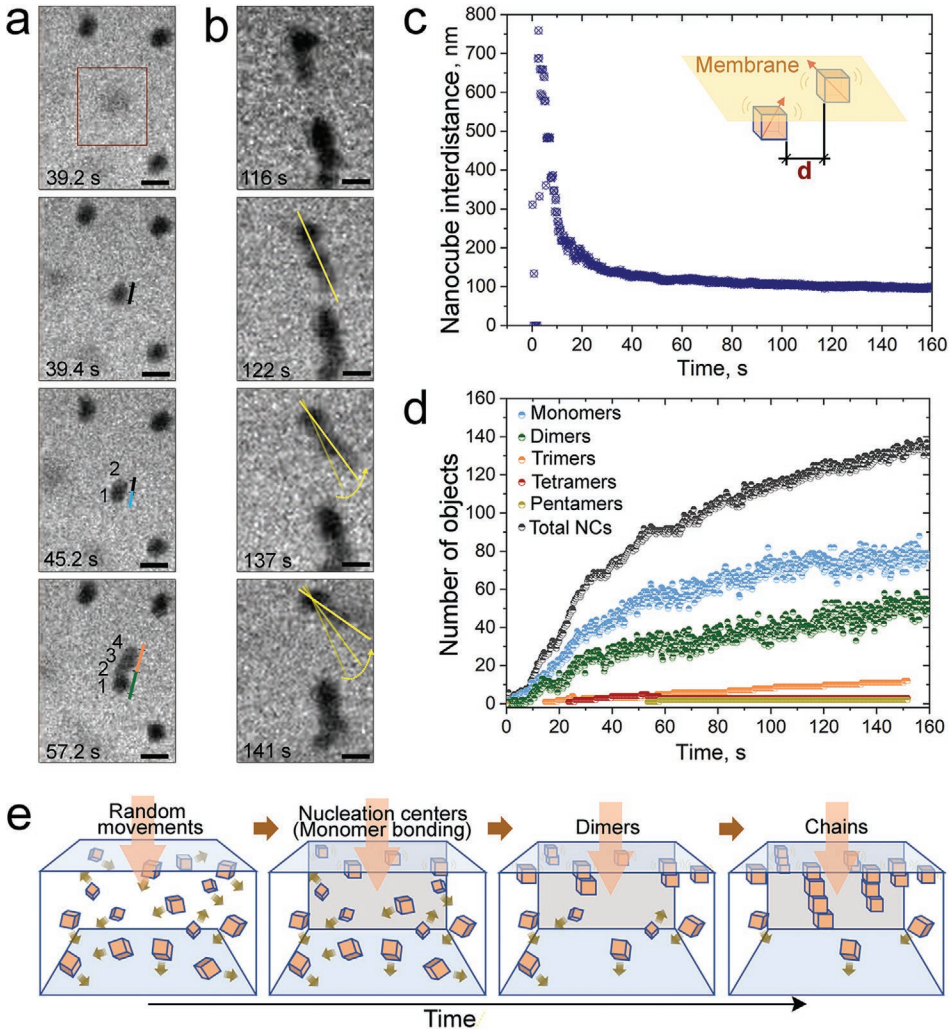

Figure 3. Tracking of nanocubes and formation of linear arrays. a) Sequence of snapshots showing the formation of a tilted chain made of four nanocubes in the red-framed region. b) Tracking the motion of a chain under focus at the top membrane. The yellow lines highlight the chain rotations over time. Scale bars: 50 nm. c) Distance *d* between closer nanocubes that remain in a fixed spatial position in the liquid cell and closer to the top membrane as a function of time. The embedded sketch indicates the measured distance among nanocubes. d) Time-dependence of the total number of single nanocubes and self-assembled arrays for an overall of 140 nanocubes in the FOV, a value that remains roughly constant. e) Cartoon showing the different stages observed in the formation of chains over time under electron beam irradiation represented by the pink arrow.

able to rotate freely without significant lateral displacement, as it is also observed from the initial monomers. With time, a third nanocube approaches the dimer, which attracts a fourth nanocube, ultimately resulting in the observed tetramer. More examples of chain nucleation and growth are provided in Figure S6 (Supporting Information). Interestingly, the complete TEM 2D projection sequences of the linear arrays show misaligned nanocubes within the chains, which indicates a symmetry breaking of the typical face-to-face contact that leads to well packed assemblies. This is only possible if they are strongly attracted by magnetic forces that act through their diagonal, inducing a preferential corner-to-corner contact, as it has been observed so far in only a few cases.[5c,12] Importantly, note that the chains do not move out of their initial location; they remain linked to the membrane through the initial attracted monomer. Moreover, in contrast with dimers, closer-up views of long chains (≥3 nanocubes; see a representative example in Figure 3b) demonstrate that part of these structures remains mobile with significant lateral displacements. The yellow lines in the figure follow the different positions acquired by the end of the chain while the initial monomer stays in its relatively fixed position. This observation indicates i) a strong electrostatic attraction of the nanocubes to the membrane, which might be expected to become weaker with distance, allowing the (partial) motion of those particles located far from the membrane; and ii) a strong magnetic interaction among nanocubes within the chain and therefore, the chains rotate as single objects in the liquid, probably under the influence of random thermal torques.

To establish the time-dependence of the assembly process, we evaluated, from the time-lapse images, the distance, *d*, defined as the distance between a nanocube bonded to the top membrane (where the focus plane was set) and their bonded neighboring particles (that is, all of them show a relatively similar contrast in the FOV, see embedded sketch in Figure 3c),

which remain all relatively fixed in their spatial location over time. The result is shown in Figure 3c. The observed trend suggests the separation of behavior into two qualitatively different regimes. The first is characterized by a rapid development of d, which we attribute to the monomer attraction to the membrane, is followed by a decrease toward a limiting value of around 100 nm, which we associate with the advanced chain growth by the attachment of new nanocubes to these initial monomers. This behavior is fully supported by nanocube counting measurements in Figure 3d, which show that the numbers of dimers and longer nanocube structures start to increase after ≈20 s of imaging. The initial stage of a rapid decrease and stabilization of d is likely the result of substantial steric repulsion among neighboring monomers caused by their equally negatively charged surfaces, which hampers both the arrival of nanocubes nearby and their side-to-side contact (the most likely configuration deeper in the liquid layer). It is worth to mention that the top membrane is not magnetic; thus, we can neglect any magnetic effect as responsible for the initial nanocube bonding to the cell membrane. The moderate attachment of the nanocubes to the liquid cell is most likely due to the progressive positive charging of the membrane (initially negatively charged as a result of the oxygen treatment applied to the e-chips) that favors their attraction. Such a positive charge arises from the ejection of secondary electrons from the membrane, thereby generating over time a net positive charge.[23] To evidence the role of the electron radiation on the initial stage of the observed assembled, we compared the number of nanocubes per nm^2 that appear on the FOV over the first 40 s of real time (that is 8 s in the supporting Movies S1 and S2, Supporting Information) at different electron dose rates. The results are presented in Figure S7 (Supporting Information), which shows a relatively higher rate of monomer bonding to the membrane when using an electron dose of 1.40 e^- Å^{-2} s^{-1} (in blue) than when irradiating the samples with a dose of 0.55 e^- Å^{-2} s^{-1} (in red). This result is consistent with a faster surface charge of the membrane itself when exposed to the high electron dose. Also, this observation is in accordance with the work of Liu et al. where the induction of a positively charged membrane via secondary electron emission during imaging was used to initiate the attachment and eventual assembly of spherical NCs.[23] In our case, the presence of such strong attractive forces not only induces the localization of monomers close to the top membrane, but also imposes a fixed orientation of the nanocube magnetic axes. Moreover, the fact that the nanocubes used in our experiments can be considered as fully magnetically blocked at room temperature and having the anisotropy axis oriented along the NC diagonal leads to enhanced magnetostatic interactions. These magnetic interactions might favor the formation of linear arrays comprised of nanocubes oriented along the diagonal, which are visualized as TEM projections of bent or tilted arrays in the FOV. Examples of "deformed" chains of nanocubes are provided in Figure S8 (Supporting Information).

The nanocube counting data in Figure 3d show that the number of monomers counted at the membrane reaches a plateau after 80 s of imaging time (blue curve) while a continuous increase of dimers and trimers is observed in the FOV (the green and orange curves) after about 20 s of imaging time. The grey curve in the figure represents the overall number of nanocubes. The green curve shows that there are few dimers that appear at shorter time, most of which do not remain in the FOV. Also, there is a time shift for the starting of trimers with respect to dimers suggesting an induction time for their growth, likely related to the need of monomer/dimer stabilization for chain growth. This shift is also observed for longer chains (curves in red and olive green for tetramers and pentamers, respectively). We note that the number of these longer structures is significantly reduced compared to dimers and trimers. This could be due to the limited thickness of the liquid layer (around 200 nm), which can host indeed a maximum of ≈6 nanocubes contacted fully through their facets and located vertically. However, we cannot exclude that the chains may be growing lateral and deep in the liquid layer, and therefore out of the objective lens focal plane, making difficult to image and consider them. Moreover, we observe at the end of the assembly that the number of chains stays roughly constant (after around 60 s). This is presumably caused by continued, albeit diminished, inflow of nanocubes into the imaging area. After ≈100 s, the formation of dimers and trimers continues while single nanocubes in the FOV have reached a plateau at around 70 nanocubes. Therefore, at this stage most of the single nanocubes became stable while the chain formation continues. Overall, these experimental observations suggest a two-step process beginning from the appearance of the nanocubes onto the membrane driven by an attractive potential (Figure S9, Supporting Information), followed by chain growth onto those initial nucleation centers, as summarized by the sketch depicted in Figure 3e.

In order to elucidate the nature of the i) attachment of the nanocubes to the membrane and ii) the chain growth on those nanocubes, we have carried out Monte Carlo simulations considering the competition between electrostatic and magnetostatic forces. We used a model described by Okada et al.,[24] modified to include the density of charge on the membrane, σ_w, as the envisaged key parameter allowing the attachment of the nanocubes to the membrane. For the sake of simplicity, we treat it indirectly through the ζ parameter (see details in Section S3.1, Supporting Information), which is defined as

$$\zeta = \frac{q\sigma_w l}{2\varepsilon_0 k_B T} \tag{1}$$

where q is the particle charge, ε_0 is the permittivity of free space, k_B is the Boltzmann constant, T the temperature (in Kelvin), and l the nanocube edge length, as defined above. The other main variable in our model is the strength of magnetostatic interaction between the nanocubes, likely responsible of promoting chain growth after the initial attachment to the membrane. Its strength is represented by the dimensionless parameter λ

$$\lambda = \frac{\mu_0 m^2}{4\pi l^3 k_B T} \tag{2}$$

where μ_0 is the vacuum permeability and m is the magnetic moment. By systematically varying the ζ and λ parameters, we found an agreement between our model and the experimental observations in the combined range of values $\zeta \approx 0.5$–1, and $\lambda \approx 20$–30. The primary results of our simulations are shown in **Figure 4**, which displays representative snapshots of the nanocube distribution in the liquid

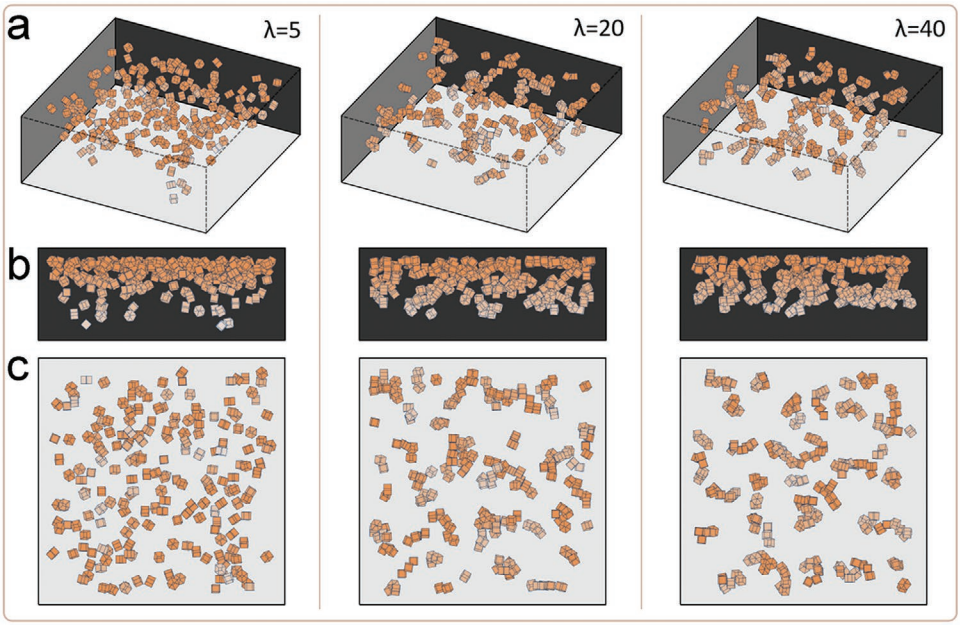

Figure 4. Dependence of the nanocube attachment and assembly. a–c) Collection of snapshots obtained from simulating the system when imposing a positively charged wall with an electric nanocube-wall interaction strength of $\zeta = 0.5$ and a magnetic nanocube interaction strength of $\lambda = 5$, 20, and 40. The panels show an oblique (a), side (b), and plane (c) views of the nanocube linear arrays assembly. The color of the cubes is graded to ease distinguishing their relative position regarding the top membrane (darker cubes are closer to the membrane and the lighter ones are progressively more separated). As the magnetic interaction strength is increased, longer chain-like assemblies are increasingly formed between the liquid cell walls.

TEM cell for different values of magnetostatic interaction λ, from 5 to 40, and imposing a membrane electric charge parameter $\zeta = 0.5$. Other parameter variations are shown in Figures S9–S11 (Supporting Information). Importantly, the good agreement between simulations and experimental results allowed estimation of the surface charge density. For the case of plotted in Figure 4, by applying Equation (1) it is obtained $\sigma_w \approx -9.0 \times 10^{-5}$ Cm^{-2}, which is within the expected range.[25] For small values of membrane charge $\zeta = 0.01$ (Figure S10, Supporting Information), simulations showed only a limited clustering for all interaction strengths λ, whereas for large $\zeta = 5$ (Figure S11, Supporting Information) the interaction with the membrane dominated and led to aggregation of the nanocubes on the membrane. These simulations suggest that positive electrostatic charging of the membrane is essential in order to reproduce the initial relatively homogeneous distributions of monomers experimentally observed and to avoid their aggregation (initial negative charge–not shown–prevented the chain formation). Strikingly, we observe chain assembly along the cube diagonals in our Monte Carlo modeling shown in Figure 4. The diagonal coupling between the cubes is clearly visible when increasing the magnetostatic interactions λ from 5 to 20. In addition, these simulations show that, as the interaction strength λ increases, from 20 to 40, there is a greater tendency for nanocubes to aggregate and form chain-like clusters. Hence, when the magnetic interaction dominates over the electric nanocube-cell membrane interaction, the chain-like clusters become less restricted to the membrane surface and able to extend their tails into the space between the top and bottom cell membranes.

In addition, our simulations show that there are around 6 nanocubes per chain, which is consistent with the chain lengths observed in our imaging experiments in Figure 3d, suggesting that the parameters used in the modelling take realistic values.

To understand further these observations of the kinetics of the chaining assembly process we constructed a rate equation approach, which is similar to those used in modelling adsorption processes.[26] Assuming that the initially suspended nanocubes can be considered a gas of approximately constant density, the assembly begins by the localization of nanocubes into the membrane by virtue of an attractive potential, and these monomers grow by the magnetic attraction of further nanocubes arriving from the surrounding liquid, as supported by our simulations. The simplest model, taking account of the minimum required bonding/debonding processes, shown in **Figure 5**a, defines transition rates t between the monomers, dimers, trimers, and tetramers.

For simplicity we only considered transitions, depicted as links with arrows, between structures different by one nanocube. This is justified as, for example, the transition from single nanocube to a trimer is not directly possible, and it was not also observed in our experimental observations. The time constant t_a is the adsorption time representing the nanocube bonding from the nanocrystal suspension to the membrane, t_d is the desorption time representing the debonding of the nanocube from the membrane, and the t_{ij} (t_{ji}) represent the time constants for the bonding (debonding) of the j-th nanocube onto a chain of i nanocubes. We use a master equation approach which is a set of coupled differential equations representing the time evolution of the population of each n-mer. A description of the model calculation is given in Section S3.3 (Supporting Information). The process can be understood considering the three interactions present in the system: nanocube–membrane interaction,

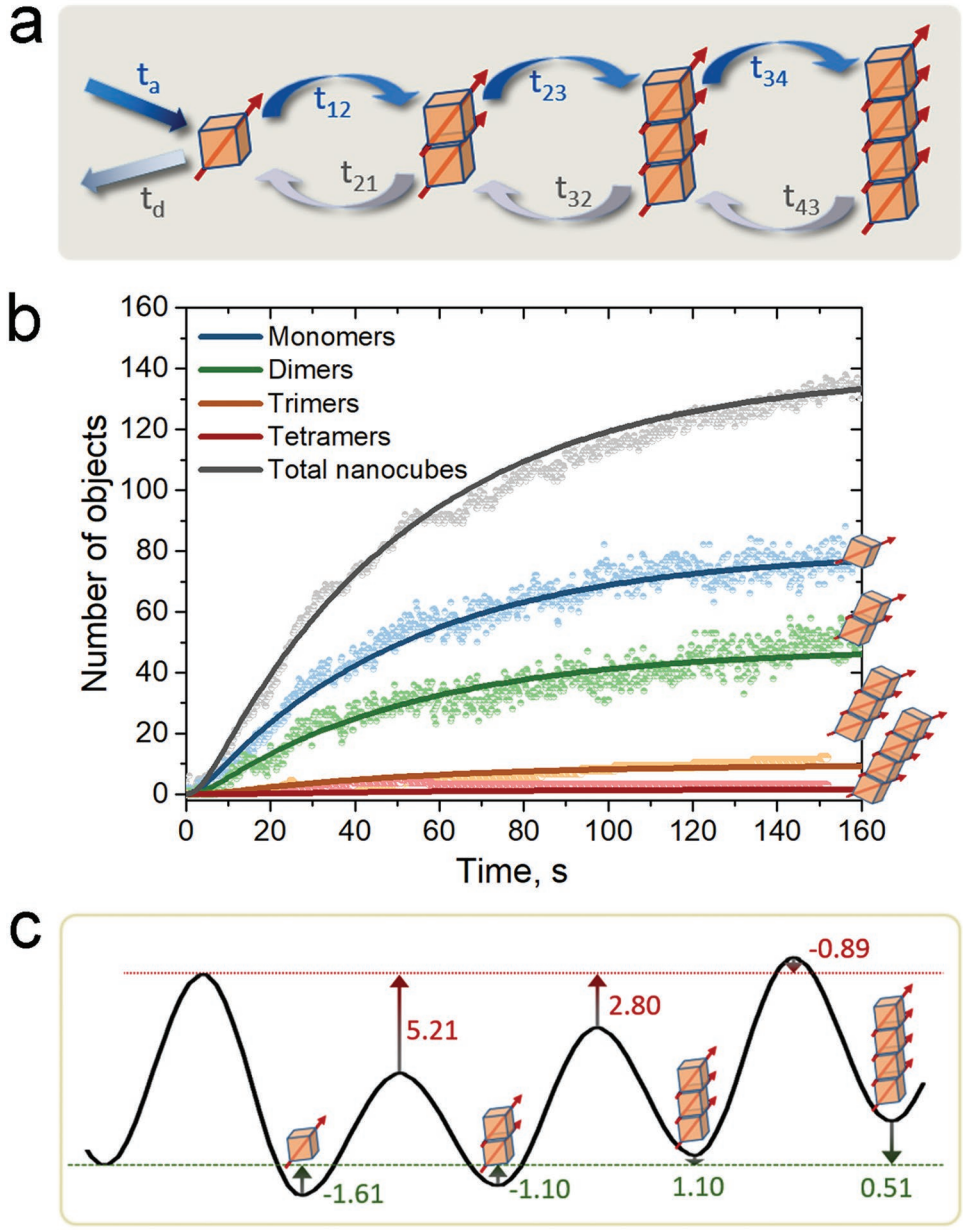

Figure 5. Master equation model: outline and predictions. a) Schematic of the allowed transitions for the thermodynamic model of the chain formation. b) Initial fit of the master equation theory to the experimental data for the number of n-mers as a function of time. c) Estimated relative energy barriers, with the associated relative energy minima, corresponding to stable chain configurations, and the energy maxima, in the units of k_BT.

nanocube–nanocube electrostatic interaction, and nanocube–nanocube magnetostatic interaction. The nanocube–nanocube magnetostatic (attractive) interaction promotes increase of the chain length, whereas the nanocube-nanocube electrostatic (repulsive) interaction prevents longer chains to be fully stable. The Equations S9 to S12 in Section S3.3 (Supporting Information) represent the transitions illustrated schematically in Figure 5a.

The initial fit to experiment is given in Figure S14 (Supporting Information). This shows an overall good agreement with experiment, but with a discrepancy for all chain lengths for small times. Specifically, the initial slope of the experimental values is smaller than that predicted by the master equation approach. This is consistent with the earlier suggestion that there is an initial phase, after the electron beam is switched on at time $t = 0$, during which the membrane charges up from its initial negative value to its maximum positive value. After the electron beam is switched on the membrane becomes increasingly positively charged due to secondary electron emission. This leads to a time-dependent value of the characteristic time (t_d) for nanocube debonding from the membrane, which we describe simply as follows. We assume transition probabilities given by an Arrhenius law, with the charging of the membrane leading to a time dependent energy barrier and consequent relaxation time. We assume a simple asymptotic increase of the

energy barrier to a maximum value with time, with the details given in Section S3.3 (Supporting Information). The fit considering this equation is shown in Figure 5b. The fit perfectly matches now the experimental data and from it we can estimate the characteristic timescales of the model, including that of the charging of the membrane during the TEM observation. Following a procedure shown in Section S3.4 (Supporting Information) we can also determine the energy barriers resulting from the nanocube-nanocube interactions. Figure 5c shows a diagram of the energy barrier landscape for the formation of the nanocube structures at the membrane. For example, considering the transition between the single cubes and the dimer structures, the energy barrier seen from the energy minimum associated with the single cube is larger than that associated with dimer structure. This implies statistically higher likelihood of dimer formation rather than dimer breakage into individual cubes. Similar observation of the energy barrier asymmetry holds for longer chains, which explains the observation of preferential chain growth, as observed in our experiments. Figure 5c also shows that the effective size of these energy barriers increases with the increasing chain length, leading to the gradual slowing down of the chain growth. This energy landscape governs the thermally activated kinetics of the chain formation process, as explained in Section S3.4 (Supporting Information). This is fully consistent with our experimental observations, demonstrated by the excellent fits of the transition state theory to our experiments in Figure 5b, and by the fact that observing longer chains (more than 6 cubes) becomes statistically unlikely due to the energy barriers growing excessively large. The fact that our master equation model describes the experiment with such accuracy strongly supports the earlier hypothesis that the observed chaining is a classical thermodynamic process involving basic routes of bonding and debonding onto nucleation centers created by the bonding of nanocubes onto the membrane–itself a gradual process as the positive charge develops on the membrane. We note that our model specifically assumes bonding/debonding of single nanocubes only. The obtained good agreement with experiments suggests that this assumption is reasonable, which is consistent with the observation that the NC suspension contains predominantly well-dispersed nanocubes.

In conclusion, we have investigated the in situ self-assembly of polymer-coated magnetic nanocubes into zig-zag linear arrays in water via liquid TEM and assessed the interplay between different types of particle interactions to explain the formation of such a peculiar assembled architecture. Through a combination of dynamic structural TEM investigations coupled with computational and theoretical studies which lays the framework for the extraction of quantitative information, we have demonstrated specifically the strength and nature of the nanocube interactions and the energy barriers to the formation of the chains. We have found that initially strong attractive electrostatic potential between the nanocubes and the liquid cell membrane-originated by the electron beam irradiation-forces some of the nanocubes to remain in a preferential orientation of their magnetic axes, acting as nucleation centers. Our combined analysis has proven that magnetic attractive interactions can overcome such electrostatic forces, favoring the arrival of neighboring nanocubes close to the nucleation centers and consecutive edge-to-edge alignment that results in the observed zig-zag assembled chains. Comparison between experiments and theoretical analysis also gives the timescale associated with the charging of the membrane and the equilibrium charge density. These results on the extent and nature of the chain assembly of magnetic nanocubes due to the influence of nanocube interactions form the bases for understanding further experimental studies in similar nanosystems, guiding them to target the creation of self-assembled tilted arrays, binary chains, 2D networks, etc. The critical knowledge that our work provides on such chain-like formation helps to bridge the gap for their implementation in nanoelectronic circuits and importantly, in hyperthermia cancer therapies where linear arrays of magnetic nanocrystals can lead to enhanced heating performances.

Experimental Section

Synthesis of PMAO-Coated $Co_{0.7}Fe_{2.3}O_4$ Nanocubes in Water: The NCs were synthesized and water transferred following previously reported protocols from the group.[18,19b,a] Details of the synthesis are provided in Section S1 (Supporting Information).

Structural and Surface Characterization: Element analysis of the PMAO-coated $Co_{0.7}Fe_{2.3}O_4$ NCs was conducted via inductive-coupled plasma spectroscopy (ICP-OES) using an iCAP 600 Thermo Fisher spectrometer. The samples were digested overnight in a HNO_3/HCl solution (1:3) and diluted in deionized water. All the suspensions were filtered before analysis by using PTFE filters.

Dynamic light scattering (DLS) and Z-potential measurements were performed on a Zetasizer Nano ZS90 instrument that is equipped with a 4.0 mW He–Ne laser operating at 632 nm and with an avalanche photodiode detector. A set of five measurements were conducted at 25 °C, with 15 acquisitions for each set.

High-resolution scanning electron microscopy analyses of the dried nanocubes were conducted on a FEI Nova 600 NanoLab instrument. Samples were prepared by drop casting (10 µL) of the nanocube suspension on Si substrates and complete water evaporation at room temperature.

In Situ TEM Experiments in Liquid: The experiments were conducted using a Protochips Poseidon 500 sample holder for liquid specimens. The NC suspensions were encapsulated between a pair of silicon chips, both with a central 50 nm thick electron-transparent Si_3N_4 membrane of 550×20 µm^2 (window size). A 150 nm-spacing between the two chips was guaranteed by metal spacers on one of the chips. The surfaces of the chips were previously plasma-treated within a Gatan Solarus 950 plasma system (15 W, 75% Ar and 25% O_2) for 120 s, after complete removal of the protective photoresist layer. A diluted suspension of the PMAO-coated $Co_{0.7}Fe_{2.3}O_4$ nanocubes was prepared by dispersing 100 µL of the synthesized NCs in 500 µL of Milli-Q water. A drop of 0.4 µL of the final suspension (15×10^{-9} M) was placed on the bottom chip to prime its surfaces and the top chip was then carefully placed with the long edge of its viewing window aligned parallel with that of the bottom chip. The liquid-containing cell was sealed, loaded in the holder, and inserted in the TEM for analysis. Next, PEEK tubes with a diameter of 300 µm were connected to the inlet and outlet of the liquid cell holder and the diluted suspension of NCs was injected at a rate of 200 µL h^{-1} by using a syringe pump. The injection of the NC suspension was interrupted as soon as few drops left the outlet, to perform the observation in static condition. The analysis started ≈30 min later, after stabilization of the liquid inside the cell.

The experiments were performed on an image-Cs-aberration-corrected JEOL JEM-2200FS TEM (Schottky source), equipped with an in-column image filter (Ω-type) and operated at 200 kV. Imaging was carried out at the lowest magnification available in the TEM range (10K x), with two different CCD cameras: a lower-dynamics, higher-noise one, observing the fluorescent screen (Hamamatsu, ORCA-ER) and allowing a wider FOV, and a higher dynamics, lower noise one (Gatan, UltraScan 1000), allowing investigation at higher spatial resolution within a smaller FOV.

All the experiments presented here were carried out in BF-TEM mode, including only the elastically scattered electrons by using a 15 eV energy-selecting slit, in order to minimize chromatic aberration. Imaging the system in unfiltered BF-TEM mode would result in a poor spatial image resolution due to strong chromatic aberration. In the experiments, there is an enhanced contrast and spatial resolution thanks to the use of an objective aperture, which improves the atomic number and diffraction contrast, and by filtering the elastically scattered transmitted electrons.[27] Electron dose rates were kept as low as possible to allow for reasonable contrast and varied in a range from 0.55 to 1.40 e^{-} $Å^{-2}$ s^{-1}. The time-lapse images were recorded from different regions in the liquid cell, with a fixed rate (≈1 frame per second, fps). All the movies included as Supporting Information are played at 5 fps. The extracted snapshots were analyzed by identifying the position, area, and aspect ratio of the objects observed in the FOV using ImageJ 1.4v. Specifically, the TEM projected aspect ratio was used of the observed structures in the FOV for each frame of the movies, by using built-in thresholds and particle analysis in the software. From these values the number of nanocubes for each object was extracted. It was found 1.4 as the threshold between monomers and dimers, and 2.4 between dimers and trimers. A survey of longer chains was directly performed on the snapshots using ROI manager in ImageJ.

Computational Modelling: To simulate the physical process the initial conditions were taken as a randomly distributed system of nanocubes (for a total of 200 NCs), each with its magnetic moment fixed along one long diagonal.[24] The nanocube positions and orientations are governed by the Metropolis algorithm, considering the evolution of the electrostatic and magnetostatic energies and assuming the experimental values: nanocubes with a lateral size, l, of ≈27 nm, a distance between membranes of around 150 nm, the experimental volume sample fraction is 2.5%, and an infinite in-plane dimension (periodic boundary conditions). Since these parameters are kept fixed throughout the simulation to investigate the role of the electrostatic and magnetostatic energies, it is convenient to rewrite electrostatic and magnetostatic energy equations (Equations S1 and S2 in Section S3.1, Supporting Information) in a compact dimensionless form, firstly for the NC/membrane interaction

$$U_i^{(q-wall)*} = \frac{U_i^{(q-wall)}}{k_B T} = \zeta z^*, \tag{3}$$

where $\zeta = \frac{q\sigma_w l}{2\varepsilon_0 k_B T}$ and $z^* = z/l$,

and secondly for the magnetostatic interaction

$$U_{ij}^{(m)*} = \frac{U_{ij}^{(m)}}{k_B T} = \lambda \frac{1}{r_{ij}^{*3}} \left\{ \hat{m}_i \cdot \hat{m}_j - \left(\hat{m}_i \cdot \hat{r}_{ij}\right)\left(\hat{m}_j \cdot \hat{r}_{ij}\right) \right\} \tag{4}$$

where $\lambda = \frac{\mu_0 m^2}{4\pi l^3 k_B T}$, $r_{ij}^* = r_{ij}/l$, and $\hat{m}_i$, $\hat{m}_j$, $\hat{r}_{ij}$ are the unit vectors.

The nanocubes are assumed to have the same magnetic moment with modulus $m = M_s V$, where M_s is the saturation magnetization of the nanocube and V its volume. Thus, since the experiment has fixed values of q, d, T, and M_s by systematically varying ζ and λ the competing role is investigated of the two envisaged processes for chain formation. The simulations were carried out at 4000 steps, guaranteeing convergence to an equilibrium state comparable to the experiments at long timescale. Some examples of the obtained results are shown in Figures S9–S11 (Supporting Information), varying the inter-nanocube interaction strength (i.e., λ) for different cases of electrostatic coupling (ζ = 0.01, 1.0, and 5.0). A detailed description of the master equation theory is presented in Section S3.3 (Supporting Information). Numerical results in this case were obtained using Maple.

Supporting Information

Supporting Information is available from the Wiley Online Library or from the author.

Acknowledgements

T.P. acknowledges financial support from European Union through the Horizon 2020 Starting European Research Council (ERC) grant ICARO (Contract Number 678109). M.P.A. and T.P. acknowledge financial support by the European Union's Horizon 2020 through the Research and Innovation Staff Exchange (RISE) programme under the Marie Skłodowska-Curie actions (MSCA) (Grant agreement 691185–COMPASS). The authors thank Mr. G. Pugliese and Dr. A. Sathya for sample preparation and the Clean Room Facility at the Istituto Italiano di Tecnologia for technical support on the liquid cell preparation. The authors also acknowledge useful discussions with Prof. Roland Kroeger. D.S. acknowledges Xunta de Galicia for financial support under the I2C Plan and the Strategic Grouping in Materials (AeMAT; Grant No. ED431E2018/08). Financial support of the Royal Society through International Exchanges scheme IE160535 is gratefully acknowledged. This work made use of computational facilities funded by the Small items of research equipment at the University of York ENERGY (Grant No. EP/K031589/1).

Conflict of Interest

The authors declare no conflict of interest.

Keywords

anisotropic nanocrystals, assembly, in situ liquid TEM, magnetic nanocubes

Received: December 18, 2019
Revised: February 23, 2020
Published online:

[1] a) M. A. Boles, M. Engel, D. V. Talapin, *Chem. Rev.* **2016**, *116*, 11220; b) A. Castelli, J. de Graaf, S. Marras, R. Brescia, L. Goldoni, L. Manna, M. P. Arciniegas, *Nat. Commun.* **2018**, *9*, 1141; c) T. Paik, C. B. Murray, *Nano Lett.* **2013**, *13*, 2952; d) Y. Taniguchi, M. A. B. Sazali, Y. Kobayashi, N. Arai, T. Kawai, T. Nakashima, *ACS Nano* **2017**, *11*, 9312; e) K. Liu, E. Kumacheva, *Nat. Mater.* **2017**, *16*, 883.

[2] a) C. Hao, L. Xu, M. Sun, W. Ma, H. Kuang, C. Xu, *Adv. Funct. Mater.* **2018**, *28*, 1802372; b) S.-Y. Zhang, M. D. Regulacio, M.-Y. Han, *Chem. Soc. Rev.* **2014**, *43*, 2301; c) K. Thorkelsson, P. Bai, T. Xu, *Nano Today* **2015**, *10*, 48; d) F. Mazuel, S. Mathieu, R. Di Corato, J.-C. Bacri, T. Meylheuc, T. Pellegrino, M. Reffay, C. Wilhelm, *Small* **2017**, *13*, 1701274.

[3] a) M. P. Arciniegas, F. D. Stasio, H. Li, D. Altamura, L. De Trizio, M. Prato, A. Scarpellini, I. Moreels, R. Krahne, L. Manna, *Adv. Funct. Mater.* **2016**, *26*, 4535; b) T. Mokari, E. Rothenberg, I. Popov, R. Costi, U. Banin, *Science* **2004**, *304*, 1787; c) L. Lin, X. Peng, M. Wang, L. Scarabelli, Z. Mao, L. M. Liz-Marzán, M. F. Becker, Y. Zheng, *ACS Nano* **2016**, *10*, 9659; d) M. B. Ross, J. C. Ku, V. M. Vaccarezza, G. C. Schatz, C. A. Mirkin, *Nat. Nanotechnol.* **2015**, *10*, 453.

[4] a) X. Ye, J. Chen, M. Engel, J. A. Millan, W. Li, L. Qi, G. Xing, J. E. Collins, C. R. Kagan, J. Li, S. C. Glotzer, C. B. Murray, *Nat. Chem.* **2013**, *5*, 466; b) F. Lu, K. G. Yager, Y. Zhang, H. Xin, O. Gang, *Nat. Commun.* **2015**, *6*, 6912.

[5] a) D. Niculaes, A. Lak, G. C. Anyfantis, S. Marras, O. Laslett, S. K. Avugadda, M. Cassani, D. Serantes, O. Hovorka, R. Chantrell, T. Pellegrino, *ACS Nano* **2017**, *11*, 12121; b) B. Bharti, A.-L. Fameau, M. Rubinstein, O. D. Velev, *Nat. Mater.* **2015**, *14*, 1104; c) G. Singh,

H. Chan, A. Baskin, E. Gelman, N. Repnin, P. Král, R. Klajn, *Science* **2014**, *345*, 1149.

[6] a) J. Kolosnjaj-Tabi, R. Di Corato, L. Lartigue, I. Marangon, P. Guardia, A. K. A. Silva, N. Luciani, O. Clément, P. Flaud, J. V. Singh, P. Decuzzi, T. Pellegrino, C. Wilhelm, F. Gazeau, *ACS Nano* **2014**, *8*, 4268; b) J.-H. Lee, J.-T. Jang, J.-S. Choi, S. H. Moon, S.-H. Noh, J.-W. Kim, J.-G. Kim, I.-S. Kim, K. I. Park, J. Cheon, *Nat. Nanotechnol.* **2011**, *6*, 418; c) Y. Qiu, S. Tong, L. Zhang, Y. Sakurai, D. R. Myers, L. Hong, W. A. Lam, G. Bao, *Nat. Commun.* **2017**, *8*, 15594.

[7] a) W. E. Mahmoud, L. M. Bronstein, F. Al-Hazmi, F. Al-Noaiser, A. A. Al-Ghamdi, *Langmuir* **2013**, *29*, 13095; b) B. Gleich, J. Weizenecker, *Nature* **2005**, *435*, 1214.

[8] a) M. E. Materia, P. Guardia, A. Sathya, M. Pernia Leal, R. Marotta, R. Di Corato, T. Pellegrino, *Langmuir* **2015**, *31*, 808; b) D. F. Coral, P. Mendoza Zélis, M. Marciello, M. d. P. Morales, A. Craievich, F. H. Sánchez, M. B. Fernández van Raap, *Langmuir* **2016**, *32*, 1201; c) S. K. Avugadda, M. E. Materia, R. Nigmatullin, D. Cabrera, R. Marotta, T. F. Cabada, E. Marcello, S. Nitti, E. J. Artés-Ibañez, P. Basnett, C. Wilhelm, F. J. Teran, I. Roy, T. Pellegrino, *Chem. Mater.* **2019**, *31*, 5450.

[9] a) M. Rycenga, J. M. McLellan, Y. Xia, *Adv. Mater.* **2008**, *20*, 2416; b) O. Rabin, *Nat. Nanotechnol.* **2012**, *7*, 419.

[10] a) L. Wu, P.-O. Jubert, D. Berman, W. Imaino, A. Nelson, H. Zhu, S. Zhang, S. Sun, *Nano Lett.* **2014**, *14*, 3395; b) K. Butter, P. H. H. Bomans, P. M. Frederik, G. J. Vroege, A. P. Philipse, *Nat. Mater.* **2003**, *2*, 88; c) M. Wang, L. He, Y. Yin, *Mater. Today* **2013**, *16*, 110; d) E. Wetterskog, C. Jonasson, D.-M. Smilgies, V. Schaller, C. Johansson, P. Svedlindh, *ACS Nano* **2018**, *12*, 1403.

[11] B. Gao, G. Arya, A. R. Tao, *Nat. Nanotechnol.* **2012**, *7*, 433.

[12] L. Balcells, I. Stanković, Z. Konstantinović, A. Alagh, V. Fuentes, L. López-Mir, J. Oró, N. Mestres, C. García, A. Pomar, B. Martínez, *Nanoscale* **2019**, *11*, 14194.

[13] a) K. L. Gurunatha, S. Marvi, G. Arya, A. R. Tao, *Nano Lett.* **2015**, *15*, 7377; b) D. Serantes, K. Simeonidis, M. Angelakeris, O. Chubykalo-Fesenko, M. Marciello, M. d. P. Morales, D. Baldomir, C. Martinez-Boubeta, *J. Phys. Chem. C* **2014**, *118*, 5927.

[14] a) B. H. Kim, J. Yang, D. Lee, B. K. Choi, T. Hyeon, J. Park, *Adv. Mater.* **2018**, *30*, 1703316; b) C. Zhang, K. L. Firestein, J. F. S. Fernando, D. Siriwardena, J. E. von Treifeldt, D. Golberg, *Adv. Mater.* **2020**, *32*, 1904094.

[15] a) X. Ye, M. R. Jones, L. B. Frechette, Q. Chen, A. S. Powers, P. Ercius, G. Dunn, G. M. Rotskoff, S. C. Nguyen, V. P. Adiga, A. Zettl, E. Rabani, P. L. Geissler, A. P. Alivisatos, *Science* **2016**, *354*, 874; b) K. L. Jungjohann, S. Bliznakov, P. W. Sutter, E. A. Stach, E. A. Sutter, *Nano Lett.* **2013**, *13*, 2964; c) J. Park, H. Elmlund, P. Ercius, J. M. Yuk, D. T. Limmer, Q. Chen, K. Kim, S. H. Han, D. A. Weitz, A. Zettl, A. P. Alivisatos, *Science* **2015**, *349*, 290; d) N. D. Loh, S. Sen, M. Bosman, S. F. Tan, J. Zhong, C. A. Nijhuis, P. Král, P. Matsudaira, U. Mirsaidov, *Nat. Chem.* **2016**, *9*, 77.

[16] a) E. Sutter, P. Sutter, A. V. Tkachenko, R. Krahne, J. de Graaf, M. Arciniegas, L. Manna, *Nat. Commun.* **2016**, *7*, 11213; b) F. Novotný, P. Wandrol, J. Proška, M. Šlouf, *Microsc. Microanal.* **2014**, *20*, 385.

[17] N. Ahmad, D. Keller, M. D. Rossell, R. Erni, *Chimia* **2018**, *72*, 727.

[18] A. Sathya, P. Guardia, R. Brescia, N. Silvestri, G. Pugliese, S. Nitti, L. Manna, T. Pellegrino, *Chem. Mater.* **2016**, *28*, 1769.

[19] a) T. Pellegrino, L. Manna, S. Kudera, T. Liedl, D. Koktysh, A. L. Rogach, S. Keller, J. Rädler, G. Natile, W. J. Parak, *Nano Lett.* **2004**, *4*, 703; b) R. Di Corato, A. Quarta, P. Piacenza, A. Ragusa, A. Figuerola, R. Buonsanti, R. Cingolani, L. Manna, T. Pellegrino, *J. Mater. Chem.* **2008**, *18*, 1991.

[20] a) E. Sutter, K. Jungjohann, S. Bliznakov, A. Courty, E. Maisonhaute, S. Tenney, P. Sutter, *Nat. Commun.* **2014**, *5*, 4946; b) A. Hutzler, B. Fritsch, M. P. M. Jank, R. Branscheid, R. C. Martens, E. Spiecker, M. März, *Adv. Mater. Interfaces* **2019**, *6*, 1970126.

[21] a) E. Sutter, B. Zhang, S. Sutter, P. Sutter, *Nanoscale* **2019**, *11*, 34; b) P. Sutter, B. Zhang, E. Sutter, *Nanoscale* **2018**, *10*, 12674.

[22] a) L. Lartigue, D. Alloyeau, J. Kolosnjaj-Tabi, Y. Javed, P. Guardia, A. Riedinger, C. Péchoux, T. Pellegrino, C. Wilhelm, F. Gazeau, *ACS Nano* **2013**, *7*, 3939; b) J. Volatron, J. Kolosnjaj-Tabi, Y. Javed, Q. L. Vuong, Y. Gossuin, S. Neveu, N. Luciani, M. Hémadi, F. Carn, D. Alloyeau, F. Gazeau, *Sci. Rep.* **2017**, *7*, 40075.

[23] Y. Liu, X.-M. Lin, Y. Sun, T. Rajh, *J. Am. Chem. Soc.* **2013**, *135*, 3764.

[24] K. Okada, A. Satoh, *Mol. Phys.* **2018**, *116*, 2300.

[25] R. F. Egerton, *Micron* **2019**, *119*, 72.

[26] Y. Liu, L. Shen, *Langmuir* **2008**, *24*, 11625.

[27] N. de Jonge, L. Houben, R. E. Dunin-Borkowski, F. M. Ross, *Nat. Rev. Mater.* **2019**, *4*, 61.